



Reducing distortions in echo-planar breast imaging at ultrahigh field with high-resolution off-resonance maps

Michael J. van Rijssel¹  | Frank Zijlstra¹  | Peter R. Seevinck¹ | Peter R. Luijten¹ | Kenneth G. A. Gilhuijs¹ | Dennis W. J. Klomp¹ | Josien P. W. Pluim^{1,2}

¹Center for Image Sciences, UMC Utrecht, Utrecht, The Netherlands

²Department of Biomedical Engineering, Technische Universiteit Eindhoven, Eindhoven, The Netherlands

Correspondence

Michael J. van Rijssel, University Medical Center Utrecht, Heidelberglaan 100, Room Q.02.4.45, 3584 CX Utrecht, The Netherlands.
Email: mrijss2@umcutrecht.nl

Funding information

ZonMw, Grant/Award Number: 104003019

Purpose: DWI is a promising modality in breast MRI, but its clinical acceptance is slow. Analysis of DWI is hampered by geometric distortion artifacts, which are caused by off-resonant spins in combination with the low phase-encoding bandwidth of the EPI sequence used. Existing correction methods assume smooth off-resonance fields, which we show to be invalid in the human breast, where high discontinuities arise at tissue interfaces.

Methods: We developed a distortion correction method that incorporates high-resolution off-resonance maps to better solve for severe distortions at tissue interfaces. The method was evaluated quantitatively both *ex vivo* in a porcine tissue phantom and *in vivo* in 5 healthy volunteers. The added value of high-resolution off-resonance maps was tested using a Wilcoxon signed rank test comparing the quantitative results obtained with a low-resolution off-resonance map with those obtained with a high-resolution map.

Results: Distortion correction using low-resolution off-resonance maps corrected most of the distortions, as expected. Still, all quantitative comparison metrics showed increased conformity between the corrected EPI images and a high-bandwidth reference scan for both the *ex vivo* and *in vivo* experiments. All metrics showed a significant improvement when a high-resolution off-resonance map was used ($P < 0.05$), in particular at tissue boundaries.

Conclusion: The use of off-resonance maps of a resolution higher than EPI scans significantly improves upon existing distortion correction techniques, specifically by superior correction at glandular tissue boundaries.

KEYWORDS

7T, B_0 mapping, breast, diffusion-weighted imaging, distortion correction, echo-planar imaging, off-resonance

1 | INTRODUCTION

DWI is an upcoming modality in breast oncology imaging. This technique, which sensitizes the MR signal for the (microscopic) motion of water molecules, has achieved promising results in recent years. Without the need for contrast agents, it potentially allows differentiation between benign and malignant lesions and prediction of response to neoadjuvant chemotherapy.^{1,2} Despite these promising feats, currently DCE-MRI is still the dominant MRI modality in breast radiology. Recent examples for the added value of tumor heterogeneity assessment include the observation that rim-enhancing tumors are a predictor for worst survival in patients with triple-negative tumors and a study that showed the value of the combination of temporal and morphological tumor characteristics in predicting treatment failure.^{3,4}

Given the promising results obtained in DCE-MRI, recent studies have tried to assess the added value of tumor heterogeneity on DWI. Promising results have been achieved in the improvement of benign/malignant differentiation and the prediction of tumor proliferation status.^{5,6} In these studies, the degree of heterogeneity has been obtained either with qualitative measures or through manually drawn tumor regions on the DWI.

Analysis of heterogeneity on DWI is severely hampered by the geometric distortions that arise in most DWI acquisitions. The vast majority of DWI acquisitions use the conventional Stejskal-Tanner approach with an EPI readout.⁷ EPI acquisitions suffer from extremely low bandwidth in the phase-encode direction, which makes them prone to severe distortion artefacts due to B_0 inhomogeneities.⁸ Additionally, because the readout bandwidth decreases with increasing resolution, the geometric distortion artefact limits the resolution of DWI in practice. Especially at ultrahigh field, this limit is reached long before the SNR limit. Due to the geometric distortion artefact, the acquired DWI data are no longer aligned with other MRI data less prone to distortions, hampering the analysis of tumor heterogeneity on DWI data and the integration of these data with, for example, DCE-MRI data, in a true multiparametric analysis of MRI.

Although several correction methods are available that attempt to recover undistorted images, all assume that main magnetic field off-resonance (ΔB_0) is locally smooth.⁹ As we will show, this assumption of locally smooth ΔB_0 is not valid in the human breast. In lipid-rich organs such as the human breast, off-resonance effects are worsened by highly discontinuous static-field inhomogeneities at tissue interfaces. These discontinuities are caused by susceptibility differences between adipose tissues and aqueous glandular tissues. Although breast tumors nearly always reside in glandular tissue, most are located on these interfaces with adipose tissue.^{10,11} The significance of these local susceptibility-

induced off-resonance effects will be demonstrated in this work. We use an ultrahigh field strength of 7 tesla (T) because DWI data are affected more by this artifact with increasing field strength.

Because we cannot assume locally smooth ΔB_0 , we develop a novel EPI distortion correction technique based on an inverse-problem strategy that is free of this assumption and works with off-resonance maps of sufficiently high resolution to capture ΔB_0 discontinuities at tissue interfaces.^{12,13} Then, we test the hypothesis that the conformity between the corrected image and a high-bandwidth reference improves using this technique.

In this paper, we will describe 3 experiments. First, in silico simulations were performed to assess the effect of susceptibility on ΔB_0 in an otherwise perfectly homogenous environment. Second, ex vivo 7T MRI measurements of ΔB_0 were performed in an ex vivo porcine tissue phantom to confirm our in silico findings. Finally, in vivo measurements of 5 healthy human volunteers were performed to test our hypothesis and novel distortion correction method in a hospital setting.

2 | METHODS

2.1 | In silico simulations

In silico simulations were performed to show the extent of local off-resonance effects caused solely by the susceptibility difference between glandular tissue and adipose tissue. A 3D unilateral breast model was created based on a 7T MRI scan of a 27-year-old healthy female volunteer. The subject was scanned with a dual-echo gradient-echo Dixon acquisition (acquired resolution $1.5 \times 1.5 \times 1.5 \text{ mm}^3$, TR 5.4 ms, in-phase TE 1.48 ms, out-phase TE 3.95, readout bandwidth 2278 Hz). Based on the Dixon in-phase, water, and fat reconstructions, a 3D susceptibility model of the volunteer's breast was constructed using tabulated values for air, water, and fat: 0.36×10^{-6} for air, -9.05×10^{-6} for water, and -7.8×10^{-6} for fat.^{14,15} From this 3D susceptibility model, local ΔB_0 variation in an external magnetic field of 7T was predicted using the method outlined in Ref. 16.

2.2 | Ex vivo measurements

Ex vivo high-resolution measurements of off-resonance in a porcine tissue phantom were used here as a model for breast tissue. The many muscle-fat interfaces present allowed us to investigate whether our findings in the simulations of high discontinuities in ΔB_0 could also be observed in an animal model. Additionally, because the specimen is completely stationary, this allowed us to develop a high-resolution ΔB_0 -based EPI distortion correction algorithm without having to take subject motion into account.

All experiments were performed using a unilateral breast coil setup on a 7T whole-body MR system (Achieva; Philips, Cleveland, OH). The protocol included 2 fat-suppressed spin-echo EPI acquisitions with opposed phase-encoding directions ($2 \times 2 \times 3 \text{ mm}^3$, bandwidth/voxel 20 Hz), a nonaccelerated spin-echo acquisition with otherwise equal imaging parameters as a reference, and a dual-echo ΔB_0 measurement at a higher resolution ($0.7 \times 0.7 \times 3 \text{ mm}^3$). In order to avoid lipid bias in the off-resonance measurements, the TEs at which the ΔB_0 map was measured were chosen such that a lipid model consisting of the 10 largest resonances was in phase with the water signal.¹⁷ Because high discontinuities in off-resonance might occur at tissue interfaces, we chose a gradient echo technique with short TEs to counter potential signal dropout in the ΔB_0 maps. Only at very large susceptibility differences, for example, close to metallic implants, the ΔB_0 maps may experience intra-voxel dephasing. This is rare in the breast because metallic implants are not common in this organ. In such cases, the EPI scans will also suffer from signal loss, which cannot be recovered by our correction method. Detailed scan parameters for all scans can be found in Table 1.

EPI distortion correction was applied as described in section 2.4.1 of this paper to pairs of oppositely encoded images using the ΔB_0 map measured at $0.7 \times 0.7 \times 3 \text{ mm}^3$, either down-sampled to the EPI resolution ($2 \times 2 \times 3 \text{ mm}^3$) or at the native ΔB_0 map resolution ($0.7 \times 0.7 \times 3 \text{ mm}^3$) that better captures local ΔB_0 discontinuities at tissue interfaces. The resulting images were compared quantitatively to the nonaccelerated reference scan as described in section 2.5 of this paper.

2.3 | In vivo measurements

All experiments conducted were in accordance with the guidelines of the local ethical committee and, written informed consent was obtained from all volunteers prior to the examination. In vivo measurements were performed in 5 healthy female volunteers (age mean: 30, range: 25–46 years) using the same 7T setup as described in section 2.2 of this paper. The in vivo acquisition protocol was nearly identical to the ex vivo acquisition protocol outlined above, with the exception that the ΔB_0 map resolution was slightly reduced. We acquired a ΔB_0 map at $1 \times 1 \times 3 \text{ mm}^3$, a set of opposite phase-encoded EPI images at $2 \times 2 \times 3 \text{ mm}^3$, and an undistorted reference scan at the same resolution. Other scan parameters were chosen as in the ex vivo case; detailed scan parameters are reported in Table 1.

Because there might be motion between the 2 EPI acquisitions, a motion-correction step was added before the distortion correction algorithm developed on the ex vivo data, as described in section 2.4.2 of this paper. And because there might also be motion present between the corrected image and the reference spin-echo scan, a rigid registration is

TABLE 1 Summary of scan parameters per sequence

Sequence	TR (ms)	TE (ms)	Resolution	Matrix Size	Readout Bandwidth (Hz)	EPI Bandwidth (Hz)	EPI Direction	EPI Factor	Scan Time (min:s)
<i>Ex-vivo scans</i>									
SE-EPI	3761	53	$2 \times 2 \text{ mm}^2$ 3 mm slices	80×80 15 slices	2807	23.7	LR/RL	80	0:08
SE ref.	3761	53	$2 \times 2 \text{ mm}^2$ 3 mm slices	80×80 15 slices	3217	–	–	–	5:08
DE GE ΔB_0 map	5.6	2.92, 3.94	$0.7 \times 0.7 \text{ mm}^2$ 3 mm slices	224×224 15 slices	1219	–	–	–	0:32
<i>In-vivo scans</i>									
SE-EPI	3761	53	$2 \times 2 \text{ mm}^2$ 3 mm slices	80×80 15 slices	2036	20.1	LR/RL	80	0:08
SE ref.	3761	53	$2 \times 2 \text{ mm}^2$ 3 mm slices	80×80 15 slices	1696	–	–	–	5:08
DE GE ΔB_0 map	7.0	2.92, 3.94	$1 \times 1 \text{ mm}^2$ 3 mm slices	160×160 15 slices	636	–	–	–	0:22

ΔB_0 : main magnetic field off-resonance; DE, dual echo; GE, gradient echo; LR, left-to-right phase encoding; ref., reference scan; RL, right-to-left phase encoding; SE, spin echo.

applied to the 2 before the quantitative comparison, as outlined in section 2.5 of this paper.

2.4 | Distortion correction

2.4.1 | Ex vivo strategy

Distortion correction was performed using an inverse problem approach resembling techniques described earlier,^{12,13} adapted to allow for higher-resolution off-resonance maps than the measured EPI scan. In this approach, we strived to invert the EPI distortion process by first creating a forward model that describes how images are distorted under the influence of ΔB_0 . In order to iteratively approximate the inverse using MatLab R2017b's (Mathworks, Natick, MA) implementation of the LSQR algorithm,¹⁸ the conjugate transpose of the forward model was also constructed and used in tandem with the forward model. The forward model (A) was described using fast steady-state simulations, restricted to distortions in the phase-encode direction. These simulations were implemented using the Fourier-based off-resonance artifact simulation in the steady state method, which avoids direct calculation of the large and sparse matrix A but allows calculation of matrix-vector products.¹⁹ This formulation allows efficient evaluation of both $A(\Delta B_0)x$ (the forward model) and $A(\Delta B_0)^Hx$ (the conjugate transpose of the forward model), where A is the transformation matrix that maps undistorted to distorted space and x is the corrected image at equal or higher resolution than the measured EPI image.

The forward model was implemented for 2D slices because our acquisition is multislice. Given that the bandwidth of the slice-selective RF pulses is 2 orders of magnitude higher than the bandwidth in the phase-encode direction, this is sufficient to explain 99% of the distortions. Distortions were modeled by considering that each k-space point is affected differently by off-resonance effects depending on its sampling time. Sampling time was defined as the time difference of the acquisition of the k-space point with respect to the center of the refocused echo. Thus, the acquired k-space signal S can be described by:

$$S(k_x(t'), k_y(t')) = \int_x \int_y \left(\rho(x,y) \cdot e^{i \cdot t' \cdot 2\pi\gamma \cdot \Delta B_0(x,y)} \cdot e^{-i2\pi(k_x(t')x + k_y(t')y)} \right), \quad (1)$$

with S the measured k-space signal distorted by off-resonance effects, ρ the effective (encoded) spin density, i the imaginary unit number, t' the sampling time for the current k-space point, γ the gyromagnetic ratio, and ΔB_0 the off-resonance map for the entire slice. x and y , respectively, denote the frequency and phase-encode directions, and k_x and k_y are their Fourier counterparts. For computational efficiency, and to be able to apply the Fourier-based off-resonance artifact simulation in the steady state model, we neglected time accrual along the frequency-encode direction and assumed a

constant sampling time for each k-space line. This limits distortions to the phase-encode direction only. Thus, the forward model is defined as follows:

$$S(k_x, k_y(t')) = \sum_x \sum_y \left(\rho(x,y) \cdot e^{i \cdot t' \cdot 2\pi\gamma \cdot \Delta B_0(x,y)} \cdot e^{-i2\pi(k_x x + k_y(t')y)} \right). \quad (2)$$

Because the dependency of k_x on t' is dropped, this equation can be efficiently evaluated by using a fast Fourier transform for every k_y :

$$S(k_x, k_y(t')) = \sum_x \left(e^{-i2\pi k_x x} \sum_y \left(\rho(x,y) \cdot e^{i \cdot t' \cdot 2\pi\gamma \cdot \Delta B_0(x,y)} \cdot e^{-i2\pi k_y(t')y} \right) \right) = \mathcal{F}_x \sum_y \left(\rho(x,y) \cdot e^{i \cdot t' \cdot 2\pi\gamma \cdot \Delta B_0(x,y)} \cdot e^{-i2\pi k_y(t')y} \right), \quad (3)$$

with \mathcal{F}_x the fast Fourier transform along the frequency-encode dimension. To allow evaluation of the model with off-resonance maps of higher resolution than the EPI image, S was subsequently cropped symmetrically around the center to the same resolution as the EPI.

The conjugate transpose model can be calculated in a similar fashion, by taking the conjugate transpose operation of the steps of the forward model and performing them in inverse order on a k-space that belongs to a deformed image. The conjugate transpose operation of Equation 3 was calculated by:

$$\hat{\rho}(x,y) = \sum_{t'} \left(\mathcal{F}_x^{-1} \left(\hat{S}(k_x, k_y(t')) \cdot e^{i2\pi k_y(t')y} \right) \cdot e^{-i \cdot t' \cdot 2\pi\gamma \cdot \Delta B_0(x,y)} \right), \quad (4)$$

with \mathcal{F}_x^{-1} the inverse fast Fourier transform along the frequency encode dimension, \hat{S} a measured and zero-padded 2D EPI k-space, and $\hat{\rho}$ the result of applying the conjugate transpose model to the measured slice. Note that the summation over t' implicitly sums over k_y because k_y is a function of t' . Centered and symmetric zero-padding was applied to upscale the measured EPI k-space to the resolution of the off-resonance map.

The inverse problem was then formulated as a damped least-squares problem:

$$y = \underset{x}{\operatorname{argmin}} \left\| \begin{bmatrix} A \\ \lambda I \end{bmatrix} x - \begin{bmatrix} b \\ 0 \end{bmatrix} \right\|_2, \quad (5)$$

with y the corrected image, b the measured EPI data, I the identity matrix, and the regularization parameter λ . A range of values between 0.1 and 100 was tested for the regularization parameter λ ; the value that maximized the Pearson correlation between the corrected ex vivo image and the undistorted reference ex vivo image was chosen for both the ex vivo specimen and all in vivo subjects (see section 2.4.2). The inverse problem was solved using the LSQR algorithm in which the matrix-vector products Ax and A^Hx

were respectively described by the forward model and conjugate transpose model, as described in Equations 2–4.¹⁸

2.4.2 | In vivo strategy

The in vivo distortion correction strategy was identical to the ex vivo strategy, but a motion correction step was added to account for subject motion between the acquisitions of the opposite phase-encoded EPI images. Motion correction was applied by (arbitrarily) choosing the EPI image with left-to-right phase encoding as reference frame and estimating rigid transformation parameters for both the other EPI image and the ΔB_0 map such that they align with the first EPI image. Due to the severe geometric distortions that present themselves differently in both EPI images, regular registration strategies are unsuited for this problem. Therefore, we estimated the 12 parameters describing the 2 rigid transformations by minimizing the same error metric that was used in the distortion correction step. This was implemented using a Nelder-Mead simplex search that minimizes the residual of the LSQR EPI distortion correction algorithm's result.²⁰ Preliminary experiments showed that 2 iterations of the LSQR algorithm sufficed for this estimation. The 2 sets of rigid transformation parameters that are obtained from the Nelder-Mead search are used in the final EPI distortion correction where the LSQR algorithm is run until convergence.

2.5 | Distortion correction evaluation

Quantitative evaluation between the corrected and nondistorted images was performed with 3 comparative metrics: Dice, Pearson correlation on the entire image, and Pearson correlation on border pixels only. For Dice and border-only Pearson correlation, a mask of the “foreground” or glandular tissue pixels was needed in both the corrected and the reference image. This mask was obtained by thresholding

using Otsu's method.²¹ The Dice coefficient was calculated directly on these 2 masks. Border-only Pearson correlation was calculated on the border pixels of the mask only; these were selected using MatLab R2017b (MathWorks) implementation of the Moore-Neighbor tracing algorithm.²² Finally, a paired one-sided Wilcoxon signed rank test was performed on all quantitative metrics, comparing the values obtained with a low-resolution ΔB_0 map with the values obtained with a high-resolution ΔB_0 map, both with motion correction.

In the in vivo scans, motion may be present between the acquisition of the first EPI image (arbitrarily chosen as reference for the correction algorithm and thus of the corrected image) and the acquisition of the reference scan. Therefore, an alignment of the corrected image to the spin-echo reference was applied to allow quantitative evaluation. Rigid registration was performed using a single-resolution approach and a normalized correlation error metric using elastix.²³

3 | RESULTS

Figure 1 shows the influence of susceptibility on ΔB_0 in the breast based on our in silico experiment. Susceptibility differences between water and fat were sufficient to cause highly discontinuous transitions in ΔB_0 locally, leading to discontinuities of more than 100 Hz over distances as small as 5 mm at 7T. Note that discontinuities at tissue boundaries are especially substantial compared to the global gradient caused by the tissue–air boundary.

The ex vivo results are presented in Figures 2 through 5. The processing time of the EPI distortion correction method was roughly 5 minutes for all 15 slices using the high-resolution ΔB_0 map. Figure 2 demonstrates that local discontinuities in ΔB_0 can also be found in a porcine tissue phantom model at fat–muscle interfaces and are easily missed in low-resolution acquisitions. The value for λ that maximized the

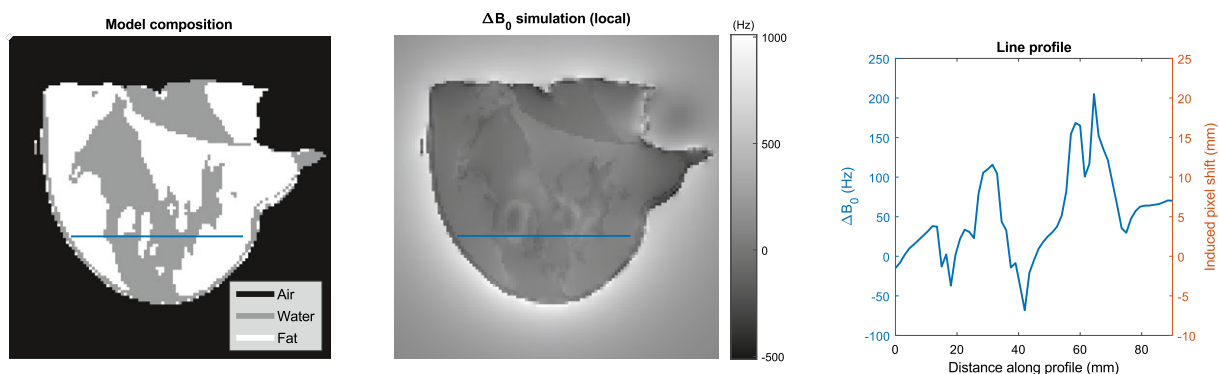


FIGURE 1 In silico experiment. Left: breast model composition based on a Dixon acquisition; gray values indicate the location of air (black), water (gray), and fat (white). Middle: simulation result of local ΔB_0 effects caused solely by susceptibility differences between tissue types at a field strength of 7T. Right: line profile corresponding to the blue line drawn in the middle panel. The y-axis is marked in both off-resonance (unit: Hz) and induced pixel shift (unit: mm) for convenience. ΔB_0 , main magnetic field off-resonance; T, tesla

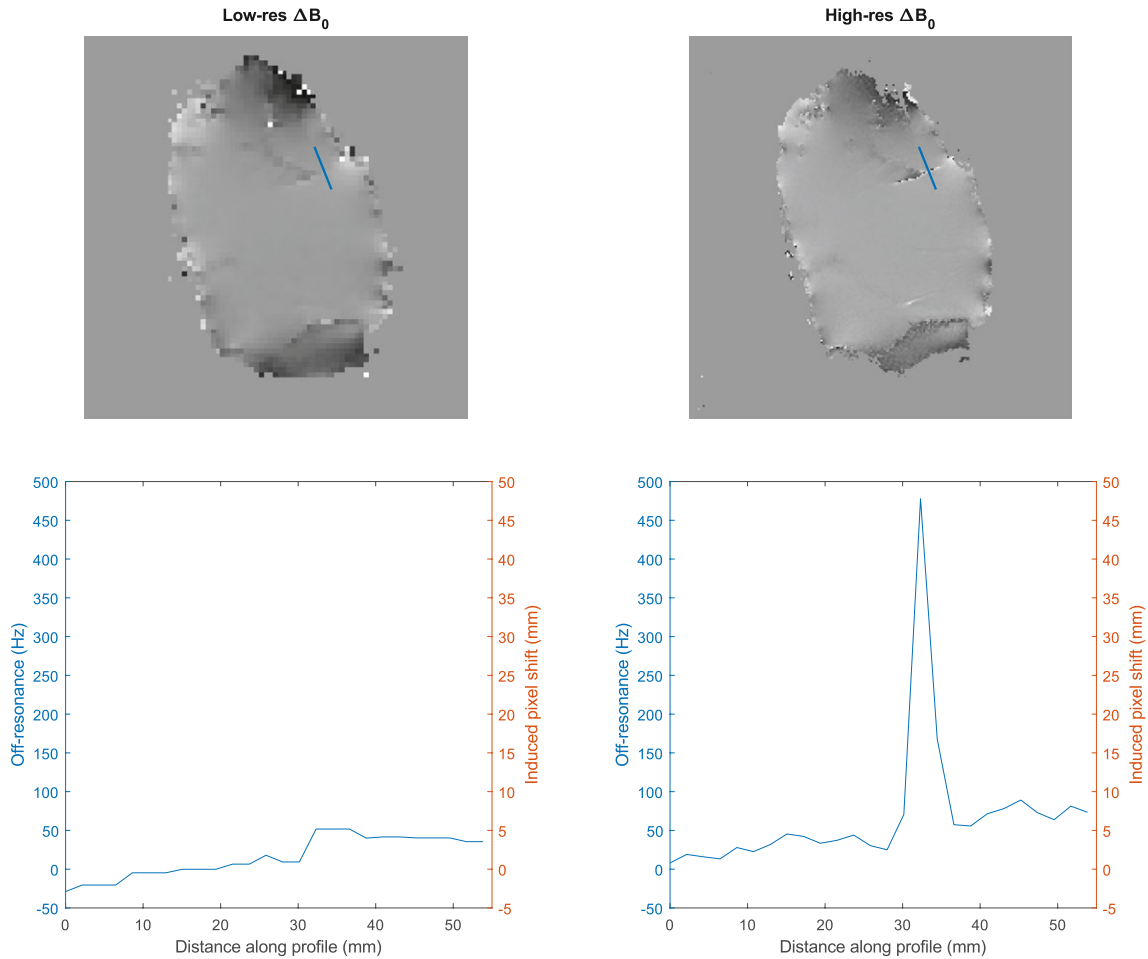


FIGURE 2 Off-resonance maps of a porcine tissue phantom acquired at different resolutions. Left: 2×2 mm in plane. Right: 0.7×0.7 mm in plane. The slice thickness was 3 mm in both cases. Notice how sharp and high discontinuities at tissue interfaces are missed in the low-resolution acquisition. The plots at the bottom indicate line profiles corresponding to the blue line drawn in the images at the top. The y-axis is marked in both off-resonance (unit: Hz) and induced pixel shift (unit: mm) for convenience

correlation between the corrected image and the reference image was 1.7. This value was used for both the ex vivo and in vivo cases. Figure 3 shows a plot of the correlation values for λ values in the range of 0.5 to 5. Note that λ has a limited influence on the correlation and, by extent, on the corrected image in this range. For values below 0.5, the correlation dropped steeply. Figure 4 shows the improvement gained by using a higher resolution ΔB_0 map during EPI distortion correction for a single slice. The image corrected with a high-resolution ΔB_0 map has less noise and more accurately depicts small features present in the reference image. Quantitative metrics are shown in Figure 5 for no correction, correction with a low-resolution ΔB_0 map, and correction with a high-resolution ΔB_0 map, respectively. All metrics improved with increasing ΔB_0 map resolutions.

The in vivo results are presented in Figures 6 through 8. The processing time for the in vivo datasets varied between the volunteers but was typically around 15 minutes per dataset (15 slices) for our combined motion and distortion

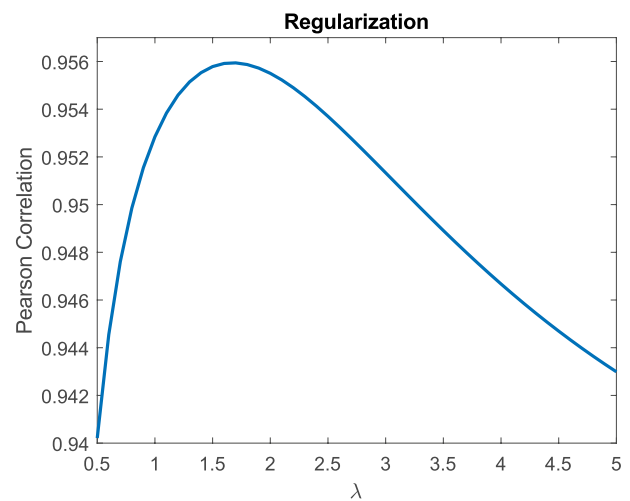


FIGURE 3 Influence of the choice of the regularization parameter λ on the Pearson correlation between the corrected and reference images in the ex vivo experiment. The maximum is located at $\lambda = 1.7$. Note the limited range of the y-axis

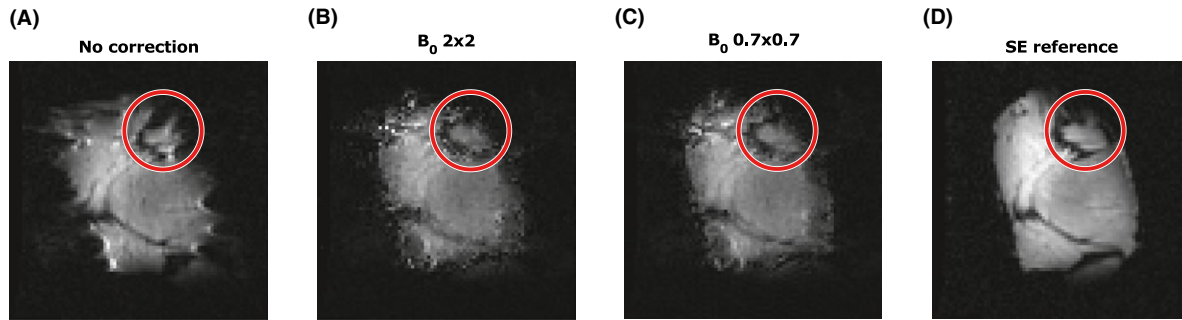


FIGURE 4 Ex vivo experiment: Uncorrected EPI (A), EPI acquisition corrected for distortion (B and C) next to an undistorted reference (D). B was corrected using a ΔB_0 map at the same resolution as the EPI acquisition (2×2 mm in plane). C was corrected using a ΔB_0 map at a higher resolution (0.7×0.7 mm in plane). Notice how C follows the anatomy of the sample more closely, especially in the red circle. Also notice the amount of signal pileup directly left of the circle is reduced in C with respect to B

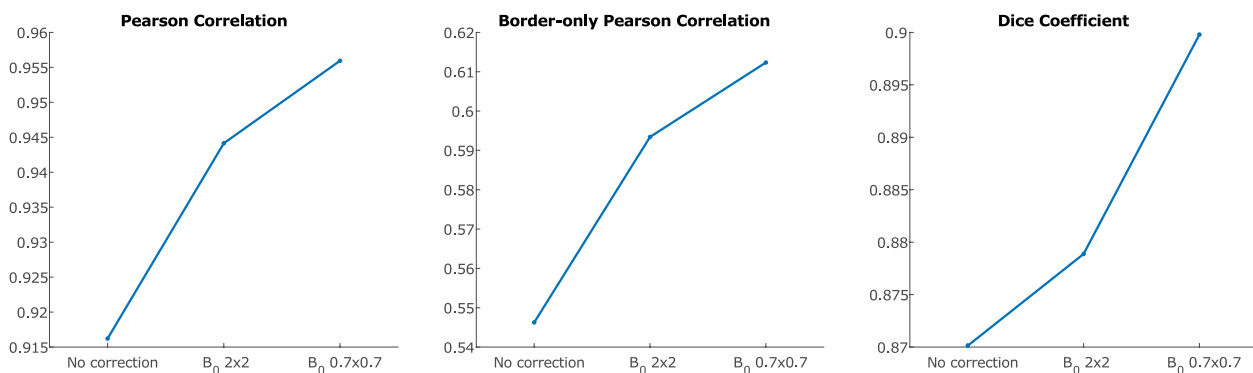


FIGURE 5 Ex vivo results of quantitative comparisons between corrected EPI images and SE references. The x-axis indicates increasing levels of sophistication for correction strategies, starting with no correction at all, then low-resolution off-resonance maps, and finally high-resolution off-resonance maps. SE, spin echo

correction strategy using the high-resolution ΔB_0 map. Figure 6 shows a side-by-side comparison of high-resolution and low-resolution ΔB_0 maps in vivo for volunteer 3. Similar to what was found in the simulations and the ex vivo scan, local discontinuities were present at tissue interfaces, which were missed in the low-resolution map. Figure 7 shows the improvement gained by using both motion correction and a higher-resolution ΔB_0 map for a single slice for volunteer 3. The difference with respect to the reference scan decreased with increasing ΔB_0 map resolution. Figure 8 shows the results of quantitative comparisons between corrected images and high-bandwidth references. Comparisons with the reference were made for noncorrected images, images corrected without motion correction and a low-resolution ΔB_0 map, images corrected with motion correction and a low-resolution ΔB_0 map, and images corrected with motion correction and a high-resolution ΔB_0 map, respectively. The *P* values that are reported resulted from a Wilcoxon signed rank test between the values obtained with a low-resolution ΔB_0 map and with a high-resolution ΔB_0 map, both with motion correction.

4 | DISCUSSION

In this study, we aimed to improve the conformity between EPI images of the breast and other MRI images less prone to distortions, such as the standard DCE-MRI. We showed that existing distortion correction methods assuming a smooth off-resonance field are inadequate due to severe field inhomogeneities that arise at tissue interfaces between aqueous and adipose tissues in the human breast. We proposed a distortion correction technique that does not assume a smooth off-resonance field and demonstrated that it performs better with increasing ΔB_0 spatial resolutions.

Our in silico results show that, even due to susceptibility alone, sizable discontinuities in off-resonance can arise at tissue interfaces between adipose and glandular tissues, making these areas prone to high distortions on EPI-based DWI. Because this is also where most breast tumors grow, it appears that many tumors would be affected by this.^{10,11}

As in the in silico simulations, highly local and sizable (up to several hundreds of Hz) discontinuities have been found both in high-resolution ex vivo scans of a porcine

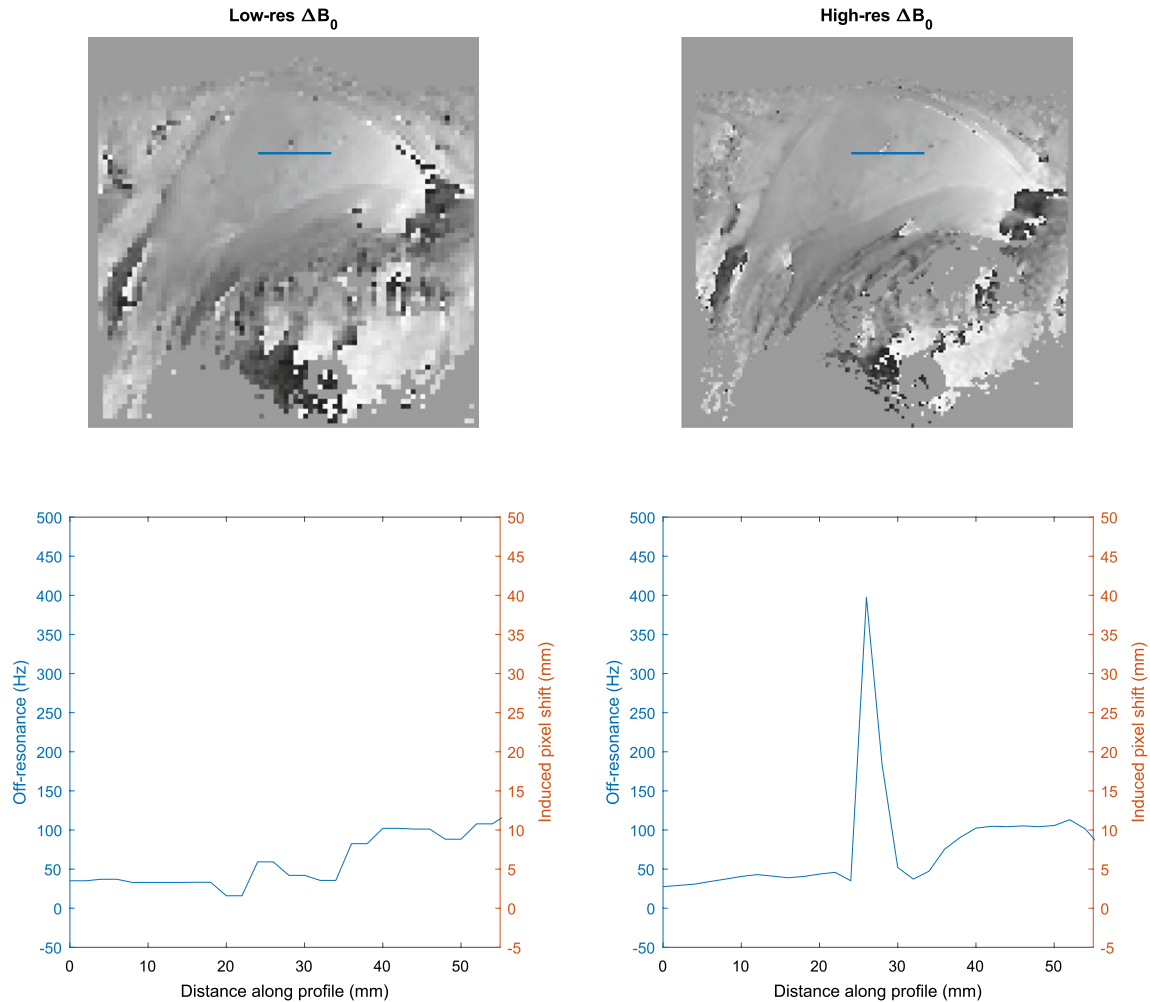


FIGURE 6 Off-resonance maps of a healthy volunteer at different resolutions. Left: 2×2 mm in plane. Right: 1×1 mm in plane. The slice thickness was 3 mm in both cases. Notice how sharp and high discontinuities at tissue interfaces are missed in the low-resolution acquisition. The plots at the bottom indicate line profiles corresponding to the blue line drawn in the images at the top. The y-axis is marked in both off-resonance (unit: Hz) and induced pixel shift (unit: mm) for convenience

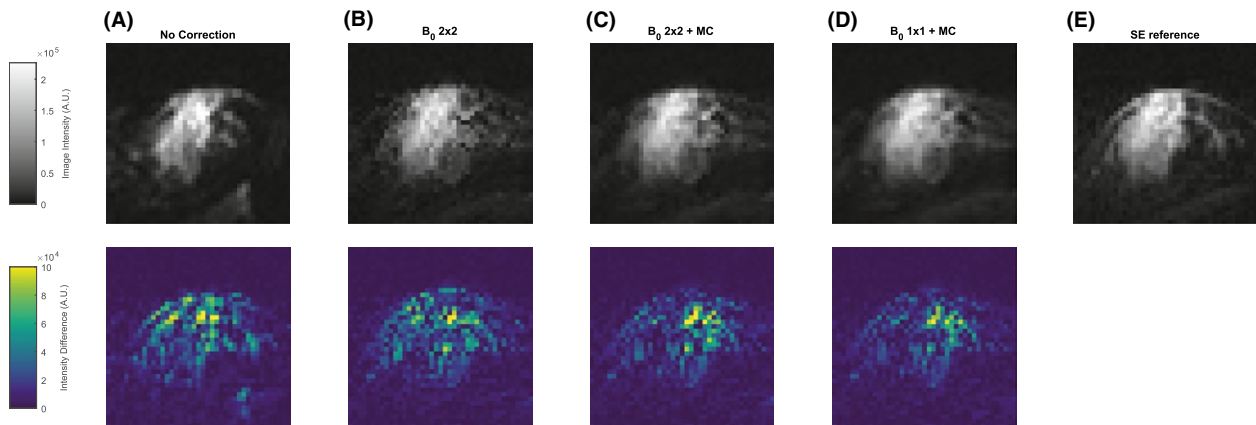


FIGURE 7 Top row: Uncorrected EPI (A), EPI acquisition corrected for distortion (B, C, and D) next to an undistorted reference (E). B was corrected using a ΔB_0 map at the same resolution as the EPI acquisition (2×2 mm in plane). C was corrected using the same ΔB_0 map, but motion correction was applied prior to distortion correction. D was corrected using a ΔB_0 map at a higher resolution (1×1 mm in plane) and motion correction. The bottom row shows the difference between each corrected image and the reference image on a different color scale

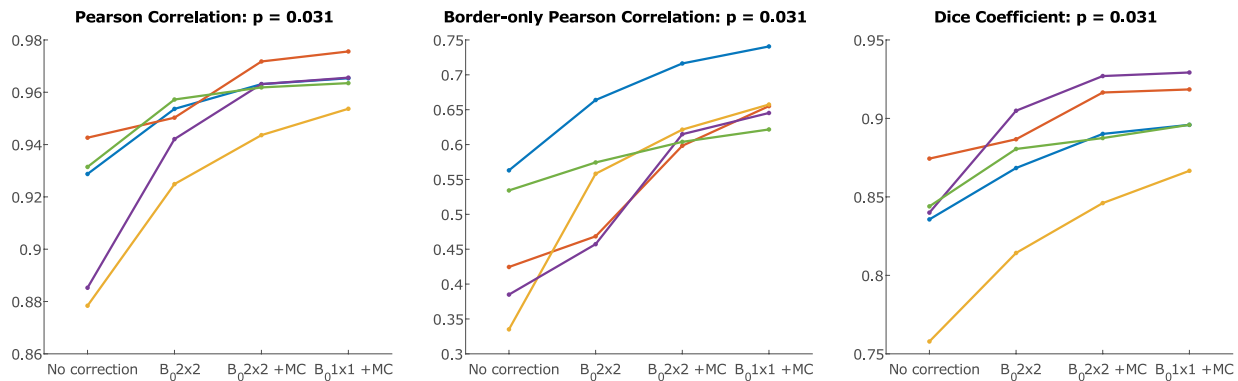


FIGURE 8 In vivo results of quantitative comparisons between corrected EPI images and SE references. The x-axis indicates increasing levels of sophistication for correction strategies, starting with no correction at all, through low-resolution off-resonance maps without and with motion correction, until high-resolution off-resonance maps with motion correction. P values indicated are obtained with a paired Wilcoxon signed rank test between the values obtained with a low-resolution ΔB_0 map and with a high-resolution ΔB_0 map, both with motion correction

tissue phantom and in high-resolution in vivo scans of healthy volunteers. These discontinuities were missed in the low-resolution scans. In traditional DWI scans, such discontinuities coincide with pixel displacements in the order of 10 cm. In fact, the ex vivo discontinuities seem to be even bigger than in our in silico results, which might be explained by the fact that muscle tissue in a porcine tissue phantom has a larger susceptibility difference with fat than human breast glandular tissue due to a higher iron content. In the simulations a tabulated value for water susceptibility is used, which may not be correct for glandular tissue; however, because in all distortion correction experiments the measured ΔB_0 maps are used, this has not influenced our results beyond the in silico simulation.

We developed a method that corrects distortion artifacts in EPI acquisitions using ΔB_0 maps at a resolution higher than the EPI images and that take subject motion into account. Both ex vivo and in vivo results demonstrate a benefit of using high-resolution ΔB_0 maps in EPI distortion correction. Although distortion correction using low-resolution ΔB_0 maps will already correct most of the distortions (e.g., observe that the Pearson correlation is higher than 0.92 for all cases with low-resolution distortion correction with motion correction in Figure 8), alignment at the edges of glandular tissue can still greatly benefit from high-resolution distortion correction. This is best demonstrated by the improvements in border-only Pearson correlation in Figure 8.

The developed method requires high-resolution ΔB_0 maps. Acquiring a high-resolution off-resonance map may be time-consuming and could be undesirable in a clinical protocol. However, in this study we managed to limit the added time to less than 30 s, which may still be acceptable in a clinical setting. In most protocols, a ΔB_0 map is already acquired for shimming purposes; simply acquiring this map with a higher resolution will satisfy the requirements of the developed method. Additionally, several techniques exist

that allow the derivation of a high-resolution ΔB_0 map from clinically relevant image sources, such as Dixon techniques in DCE MRI, which are standard in many multiparametric cancer protocols. Alternatively, a merger of low-resolution ΔB_0 maps with high-resolution simulations based on segmentations, like we performed in the first part of this work, might be a feasible solution to avoid the extra time needed for obtaining high-resolution ΔB_0 maps.

Techniques exist that estimate the ΔB_0 map directly from opposed phase-encoded data.¹³ However, these methods need to assume a smooth ΔB_0 field in order to reduce the parameter space. They also ignore the resonance and susceptibility offsets between aqueous and adipose substances. Although these assumptions are valid in, for example, the brain, we have demonstrated they are not true in the breast, justifying the development of more sophisticated methods, as we have done here. The development of a method that estimates a high-resolution ΔB_0 map from opposite phase-encoded data without the assumption of a smooth ΔB_0 field could be a viable and scan time-efficient solution, which should be investigated in future work.

Others go beyond field map estimation and try to estimate subvoxel ΔB_0 gradients in order to account for signal dephasing.²⁴ In order to be able to estimate these subvoxel effects, they designed an acquisition scheme with multiple echoes and compensation gradients in the slice-selection direction, which requires extra scan time. Validation was limited to computerized phantoms. Our forward model takes signal dephasing into account for the frequency and phase-encode directions by simulating a model that has a higher resolution than the returned image. It might be possible to extend our forward model to include dephasing in the slice-selection direction as well by simulating several thinner slices at the same time. This is beyond the scope of this paper. Additionally, the ΔB_0 map would need to be acquired with thinner slices, which increases the required scan time.

An alternative approach for EPI distortion correction is nonrigid registration to a nondistorted or less-distorted target image, for example, the DCE MRI.²⁵ Some authors have proposed combining such image registration-based methods with field-based methods, with promising results.^{26,27} It is possible to extend our method in this direction, for example, by introducing nonrigid registration after the EPI distortion correction or by interleaving these 2 steps. When using nonrigid registration techniques, there is always a risk of contaminating the corrected image with information from the target image. For example, tumor heterogeneities in the target image that are absent in the source EPI may be propagated into the corrected image or, inversely, heterogeneities present in the source EPI but absent in target image may be removed. Because a main motivation of this work is to enable assessment of tumor heterogeneity in both DCE MRI and DWI accurately and independently, we have chosen not to pursue such an approach.

There is a linear relationship between field strength and the amount of off-resonance generated by magnetic susceptibility differences. Therefore, the induced distortions will also be lower at lower field strengths, and the added benefit of our method will be less noticeable. Nevertheless, as Figure 6 demonstrates, severe discontinuities of up to 400 Hz have been found in vivo, translating into 40-mm pixel shifts with our current protocol. At 1.5T, this discontinuity would have been 86 Hz (3/14th part of 400 Hz), which would translate into a 9-mm pixel shift. At voxel sizes of roughly 2×2 mm in-plane, which are common for this kind of protocol, this is still not within acceptable limits. Therefore, we believe high-resolution ΔB_0 field information may merit distortion correction in DWI of the breast, even at more conventional field strengths.

Limitations of this study include the simplification in our distortion model to describe the phase-encode direction only. Because the readout bandwidth is roughly 2 orders of magnitude higher than the phase-encode bandwidth of our sequence (see Table 1), we believe this simplification is justified because including the readout direction in the model would hardly improve distortion prediction and correction. A second limitation is the rigid motion-correction step that was implemented to test our method in in vivo cases. Several nonrigid techniques exist; however, these techniques could potentially correct for geometric distortion artefacts left uncorrected by our method and hide errors that our method made. In order to have a clean evaluation of our method's performance, we chose to limit our motion-correction step to rigid registration only. In terms of optimization, our method uses the LSQR method with L2 regularization. We considered these an appropriate choice; however, they can be replaced by other optimizers and regularization strategies. Other optimizers might be more efficient in solving the inverse problem, and other regularizers might improve the corrected images. Lastly, we cannot specify a minimum resolution for the ΔB_0 map that our method requires because

we have not tested different resolution levels. Future studies might focus on this, but we would like to stress that an increase with a factor 2×2 in plane, as we have done for the in vivo data, already brings a significant improvement in distortion correction. As can be seen in Figure 2 for in vivo and in Figure 6 for ex vivo data, a small increase in resolution already allows the detection of severe local field inhomogeneities that are otherwise missed.

5 | CONCLUSION

Highly local and sizable (up to several hundreds of Hz) discontinuities in off-resonance have been found in the human breast at ultrahigh field, making the DWI of these regions, where most breast tumors grow, exceptionally challenging. A high-resolution off-resonance map allows integration of local ΔB_0 discontinuities at tissue interfaces to better describe image distortion at those interfaces. Although distortion correction using low-resolution off-resonance maps corrects most of the distortions, alignment at the edges of glandular tissue greatly benefits from high-resolution distortion correction. Consequently, using off-resonance maps of a resolution higher than the measured EPI scans improves the conformity between images corrected for EPI distortions and a high-bandwidth reference. This ensures distortion-corrected DWI scans spatially match to clinical DCE images, which facilitates multiparametric heterogeneity assessment.

CONFLICT OF INTEREST

Peter Seevinck is cofounder and minority shareholder of MRIguidance BV.

ORCID

Michael J. van Rijssel  <https://orcid.org/0000-0002-2365-4408>

Frank Zijlstra  <https://orcid.org/0000-0002-9184-7666>

REFERENCES

1. Woodhams R, Matsunaga K, Kan S, et al. ADC mapping of benign and malignant breast tumors. *Magn Reson Med Sci*. 2005;4:35–42.
2. Sharma U, Danishad KKA, Seenu V, Jagannathan NR. Longitudinal study of the assessment by MRI and diffusion-weighted imaging of tumor response in patients with locally advanced breast cancer undergoing neoadjuvant chemotherapy. *NMR Biomed*. 2009;22:104–113.
3. Schmitz AMT, Loo CE, Wesseling J, Pijnappel RM, Gilhuijs KGA. Association between rim enhancement of breast cancer on dynamic contrast-enhanced MRI and patient outcome: impact of subtype. *Breast Cancer Res Treat*. 2014;148:541–551.

4. Chan HM, van der Velden BHM, Loo CE, Gilhuijs KGA. Eigentumors for prediction of treatment failure in patients with early-stage breast cancer using dynamic contrast-enhanced MRI: a feasibility study. *Phys Med Biol*. 2017;62:6467–6485.
5. An YY, Kim SH, Kang BJ. Differentiation of malignant and benign breast lesions: added value of the qualitative analysis of breast lesions on diffusion weighted imaging (DWI) using readout segmented echo-planar imaging at 3.0 T. *PLoS ONE*. 2017;12:e0174681.
6. Fan M, He T, Zhang P, Zhang J, Li LH. Heterogeneity of diffusion-weighted imaging in tumours and the surrounding stroma for prediction of Ki-67 proliferation status in breast cancer. *Sci Rep*. 2017;7:2875.
7. Stejskal EO, Tanner JE. Spin diffusion measurements: spin echoes in the presence of a time-dependent field gradient. *J Chem Phys*. 1965;42:288–292.
8. Jezzard P, Balaban RS. Correction for geometric distortion in echo-planar images from B-0 field variations. *Magn Reson Med*. 1995;34:65–73.
9. Hancu I, Lee SK, Hulsey K, et al. Distortion correction in diffusion-weighted imaging of the breast: Performance assessment of prospective, retrospective, and combined (prospective plus retrospective) approaches. *Magn Reson Med*. 2017;78:247–253.
10. Stacey-Clear A, McCarthy KA, Hall DA, et al. Mammographically detected breast cancer: location in women under 50 years old. *Radiology*. 1993;186:677–680.
11. Kim WH, Li M, Han W, Ryu HS, Moon WK. The spatial relationship of malignant and benign breast lesions with respect to the fat-gland interface on magnetic resonance imaging. *Sci Rep*. 2016;6:39085.
12. Munger P, Crelier GR, Peters TM, Pike GB. An inverse problem approach to the correction of distortion in EPI images. *IEEE Trans Med Imaging*. 2000;19:681–689.
13. Andersson JLR, Skare S, Ashburner J. How to correct susceptibility distortions in spin-echo echo-planar images: application to diffusion tensor imaging. *NeuroImage*. 2003;20:870–888.
14. Schenck JF. The role of magnetic susceptibility in magnetic resonance imaging: MRI magnetic compatibility of the first and second kinds. *Med Phys*. 1996;23:815–850.
15. Hopkins JA, Wehrli FW. Magnetic susceptibility measurement of insoluble solids by NMR: magnetic susceptibility of bone. *Magn Reson Med*. 1997;37:494–500.
16. Bouwman JG, Bakker CJG. Alias subtraction more efficient than conventional zero-padding in the Fourier-based calculation of the susceptibility induced perturbation of the magnetic field in MR. *Magn Reson Med*. 2012;68:621–630.
17. Boer VO, Luttje MP, Luijten PR, Klomp DWJ. Requirements for static and dynamic higher order B0 shimming of the human breast at 7 T. *NMR Biomed*. 2014;27:625–631.
18. Paige CC, Saunders MA. LSQR: an algorithm for sparse linear equations and sparse least squares. *ACM T Math Software*. 1982;8:43–71.
19. Zijlstra F, Bouwman JG, Braskute I, Viergever MA, Seevinck PR. Fast Fourier-based simulation of off-resonance artifacts in steady-state gradient echo MRI applied to metal object localization. *Magn Reson Med*. 2017;78:2035–2041.
20. Lagarias JC, Reeds JA, Wright MH, Wright PE. Convergence properties of the Nelder-Mead simplex method in low dimensions. *Siam J Optimiz*. 1998;9:112–147.
21. Otsu N. A threshold selection method from gray-level histograms. *IEEE Trans Syst Man Cybern Syst*. 1979;9:62–66.
22. Gonzalez RC, Woods RE, Eddins SL. *Digital Image Processing Using MATLAB*. Upper Saddle River, NJ: Pearson Prentice Hall; 2004.
23. Klein S, Staring M, Murphy K, Viergever MA, Pluim JPW. elastix: a toolbox for intensity-based medical image registration. *IEEE Trans Med Imaging*. 2010;29:196–205.
24. Dagher JC, Meyer FG. A joint acquisition-reconstruction paradigm for correcting inhomogeneity artifacts in MR echo planar imaging. *Conf Proc IEEE Eng Med Biol Soc*. 2011;2011:3744–3750.
25. Mendez CA, Pizzorni Ferrarese F, Summers P, Petralia G, Menegaz G. DCE-MRI and DWI Integration for breast lesions assessment and heterogeneity quantification. *Int J Biomed Imaging*. 2012;2012:676808.
26. Gholipour A, Kehtarnavaz N, Scherrer B, Warfield SK. On the accuracy of unwarping techniques for the correction of susceptibility-induced geometric distortion in magnetic resonance echo-planar images. *Conf Proc IEEE Eng Med Biol Soc*. 2011;2011:6997–7000.
27. Irfanoglu MO, Walker L, Sammet S, Pierpaoli C, Machiraju R. Susceptibility distortion correction for echo planar images with non-uniform B-spline grid sampling: a diffusion tensor image study. *Med Image Comput Comput Assist Interv*. 2011;14:174–181.

How to cite this article: van Rijssel MJ, Zijlstra F, Seevinck PR, et al. Reducing distortions in echo-planar breast imaging at ultrahigh field with high-resolution off-resonance maps. *Magn Reson Med*. 2019;82:425–435. <https://doi.org/10.1002/mrm.27701>